Article

Voxelated soft matter via multimaterial multinozzle 3D printing

https://doi.org/10.1038/s41586-019-1736-8

Received: 21 August 2019

Accepted: 9 October 2019

Published online: 13 November 2019

Mark A. Skylar-Scott[1,2,3], Jochen Mueller[1,2,3], Claas W. Visser[1,2] & Jennifer A. Lewis[1,2*]

There is growing interest in voxelated matter that is designed and fabricated voxel by voxel[1–4]. Currently, inkjet-based three-dimensional (3D) printing is the only widely adopted method that is capable of creating 3D voxelated materials with high precision[1–4], but the physics of droplet formation requires the use of low-viscosity inks to ensure successful printing[5]. By contrast, direct ink writing, an extrusion-based 3D printing method, is capable of patterning a much broader range of materials[6–13]. However, it is difficult to generate multimaterial voxelated matter by extruding monolithic cylindrical filaments in a layer-by-layer manner. Here we report the design and fabrication of voxelated soft matter using multimaterial multinozzle 3D (MM3D) printing, in which the composition, function and structure of the materials are programmed at the voxel scale. Our MM3D printheads exploit the diode-like behaviour that arises when multiple viscoelastic materials converge at a junction to enable seamless, high-frequency switching between up to eight different materials to create voxels with a volume approaching that of the nozzle diameter cubed. As exemplars, we fabricate a Miura origami pattern[14] and a millipede-like soft robot that locomotes by co-printing multiple epoxy and silicone elastomer inks of stiffness varying by several orders of magnitude. Our method substantially broadens the palette of voxelated materials that can be designed and manufactured in complex motifs.

Physical objects can be broken down and described as a collection of finite-volume elements—that is, voxels. Voxels can be stored as a virtual *n*-dimensional matrix, the individual elements of which define the local material composition, structure and properties. Additive manufacturing offers the potential to reverse this process by generating voxelated matter from a 3D dataset in which multimaterial building blocks are assembled voxel by voxel. Although additive-manufacturing platforms, augmented by optimization[15,16] or machine-learning tools[3,4], could afford nearly unlimited design potential, the only such method that is well suited for constructing voxelated matter is inkjet-based 3D printing. This method is capable of reproducing exquisitely detailed multimaterial datasets[1–4]; however, both the number of printable materials and their properties are limited by the constraints imposed by drop-on-demand printing.

Direct ink writing (DIW) is an alternative 3D printing method that is capable of patterning a broad palette of high-performance materials; however, existing embodiments rely on extruding cylindrical filaments composed of a single material through a single nozzle in a layer-by-layer manner. An ideal multimaterial DIW system would be able to extrude a multimaterial filament at a sufficiently high switching frequency to create voxel elements (of about D^3 in volume, where D is the nozzle diameter) along its length with specified compositions. Although recent advances in the design and implementation of mixing[17,18] and switching[19,20] nozzles allow multiple materials to be co-printed continuously, the frequency or resolution at which they can switch materials is limited, and thus they are unable to produce such voxelated filaments. Specifically, the large dead volume in mixing nozzles results in long material transitions, whereas the use of flow-driven syringe pumps to operate switching nozzles limits the switching frequency (about 1 Hz) owing to compliance and thread backlash. In addition, print speed constraints that arise from printing 3D objects using single nozzles greatly limit the vast design space that can be realized by voxelated soft matter. To retain part resolution when the linear scale of a 3D object is increased by a factor of L, the number of printed voxels, as well as the build time, must be increased by L^3. This scaling behaviour is especially prohibitive for manufacturing large parts using reactive[17] or biological[21] inks with short printability windows. To reduce build times, one-dimensional (1D) multinozzle arrays have been developed, which split a single inlet stream of ink into multiple continuous ink filaments that exit simultaneously from the printhead[22]. However, because each nozzle is able to extrude only a single material, the 3D objects produced via these multinozzle arrays have limited complexity.

Here we report an MM3D printing method for generating voxelated soft matter that integrates ultrarapid multimaterial switching for enhanced complexity with multinozzle printing for enhanced build speed (Fig. 1a). Using MM3D printing, we produced complex architectures composed of multiple materials with controlled composition, function and structure in a voxel-by-voxel manner (Fig. 1a). We designed and rapidly fabricated MM3D printheads in the form of zero-dimensional (0D; single nozzle), 1D and 2D nozzle arrays using

[1]Harvard John A. Paulson School of Engineering and Applied Sciences, Harvard University, Cambridge, MA, USA. [2]Wyss Institute for Biologically Inspired Engineering, Harvard University, Cambridge, MA, USA. [3]These authors contributed equally: Mark A. Skylar-Scott, Jochen Mueller. *e-mail: jalewis@seas.harvard.edu

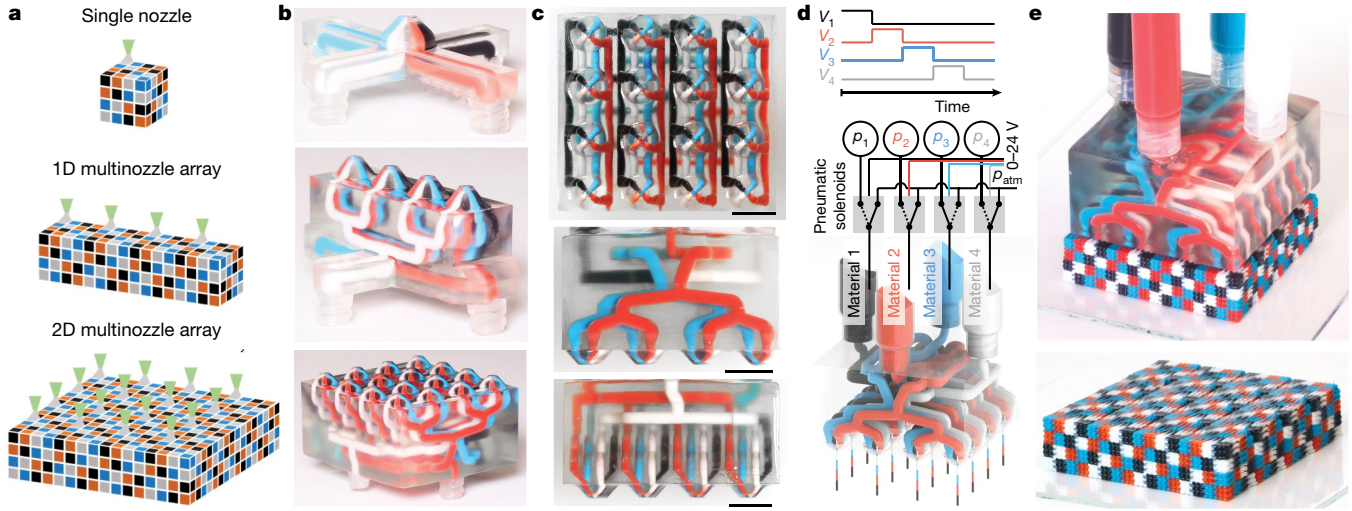

Fig. 1 | Multimaterial multinozzle 3D printheads. a, Schematic of voxelated architectures printed using a single (0D) nozzle (top) and the 1D (middle) and 2D (bottom) MM3D printheads. **b**, Photographs of the corresponding 0D, 1D and 2D four-material MM3D printheads. **c**, Photographs showing the top (top) and side (middle and bottom) views of a 4 × 4-nozzle, four-material, 2D MM3D printhead. Scale bars, 10 mm. **d**, Schematic of MM3D printhead operation, where V_1–V_4 represent the voltage waveforms controlling the extrusion pressures p_1–p_4 for materials 1–4, and p_{atm} denotes the atmospheric pressure. **e**, Voxelated matter produced by MM3D printing using a 4 × 4-nozzle, four-material, 2D printhead.

stereolithography (Fig. 1b, c, Extended Data Fig. 1a–c). These MM3D printheads are capable of depositing up to eight materials, each of which flows through independent bifurcating channel networks that reside within the printhead, before merging into a single ink flow immediately before the nozzle outlet (Extended Data Fig. 1d, e). To ensure uniform printing, each nozzle in the printhead must have an inner diameter with a coefficient of variation below about 5% (Extended Data Fig. 2)[22]. Each printhead is connected to multiple syringes, each of which contains a different material, that are actuated by a bank of fast-cycling pneumatic solenoids to enable high-frequency switching (Fig. 1d). Using this embodiment, 3D objects must be produced in periodic layouts because each nozzle is not independently switchable. Importantly, MM3D printheads are capable of generating voxelated matter at characteristic build times that scale with L, instead of L^3, for single nozzles (Fig. 1e, Supplementary Video 1, Extended Data Fig. 3; see Methods for further analysis).

Modelling multimaterial switching

A salient feature of our MM3D printheads is their S_{ink}-to-1 junctions, in which S_{ink} material channels converge into a single outlet to generate continuous, but heterogeneous, filaments, the composition and properties of which are specified at the voxel level (Fig. 2a). For MM3D printing, we opted to use pressure-driven flows to enable faster start–stop dynamics (that is, higher switching frequencies) compared to the syringe pump-driven flows used previously[19]. However, pressure-driven extrusion requires careful optimization of the ink rheology, nozzle geometry and printing pressure to prevent ink from one channel flowing upstream into a neighbouring channel that houses a different ink. If backflow occurs, then the wrong voxel composition is extruded immediately after switching. To model and optimize this parameter space, we created Y-junction nozzles and directly observed the ink flows (Fig. 2b). For Newtonian inks, the equivalent circuit would be a resistive network, where any material flow on one side would drive a backflow in the other channel, rendering MM3D printing impossible (Fig. 2c). By contrast, two viscoelastic inks—that is, Herschel–Bulkley fluids with shear yield stresses—exhibit nonlinear flow behaviour similar to that of a network of transient voltage suppressor diodes. Here, a finite flow of $Q_f < Q_f^{max}$ can occur in one channel while maintaining a static condition in the other channel, that is, $Q_s = 0$. This zero-backflow condition persists as long as the back-pressure generated at the junction, p_j, does not exceed a critical value, p_{cr}, that would result in yielding of the static material (Fig. 2d, Supplementary Video 2, Extended Data Fig. 4). We derived an analytical model for p_{cr} and found that the corresponding maximum flow rate of the ink, Q_f^{max}, depends on the channel geometry and ink rheology (see Methods for an extended discussion). To test this model, we flowed a range of silicone inks of varying viscosity and shear yield stress and experimentally detected the yielding of the static ink to quantify Q_f^{max} (Fig. 2e, Extended Data Fig. 5). As predicted, Q_f^{max} and, hence, the maximum print speed depend on the shear yield stress of the static ink and the apparent viscosity of the flowing ink (Fig. 2f). The geometry of the nozzle also affects Q_f^{max} considerably: longer inlet (Fig. 2g) or shorter outlet (Fig. 2h) channels enable higher print speeds. The use of asymmetric MM3D printheads facilitates printing of multiple inks with widely varying rheological behaviour. For example, asymmetric printheads can be designed with longer channels for the lower-viscosity ink, such that the maximum print speed for each ink is better matched to enable constant printhead movement (Fig. 2i).

MM3D printing performance

To generate continuous multimaterial filaments composed of voxelated elements, we operate the MM3D printheads at a switching frequency of up to 50 Hz (Fig. 3a, Supplementary Video 3), enabling 3D objects to be rapidly printed in a voxel-based manner. For example, using 8 × 1 1D MM3D printheads, voxelated soft matter can be generated by scanning either 'parallel' lines or by completing each 'island' of material before switching to the next (Fig. 3b, c, Extended Data Fig. 6). Compared to the island method, the parallel method enables simpler print-path design with fewer aberrations due to filament cornering. However, the island method enables fewer material transitions and therefore can generate sharper borders. When co-printing representative silicone and wax inks at high speeds, the 'more viscous' silicone ink had a propensity to backflow into the 'less viscous' wax channel (that is, $Q_{f,\,silicone}^{max} < Q_{f,\,wax}^{max}$), causing backflow aberrations (Extended Data Fig. 7). To mitigate this, we designed a matched asymmetric nozzle with a narrower channel for delivering the wax ink. A 0D asymmetric nozzle could raster arbitrary high-fidelity patterns with a single continuous filament with a diameter of 250 μm (Supplementary Video 4).

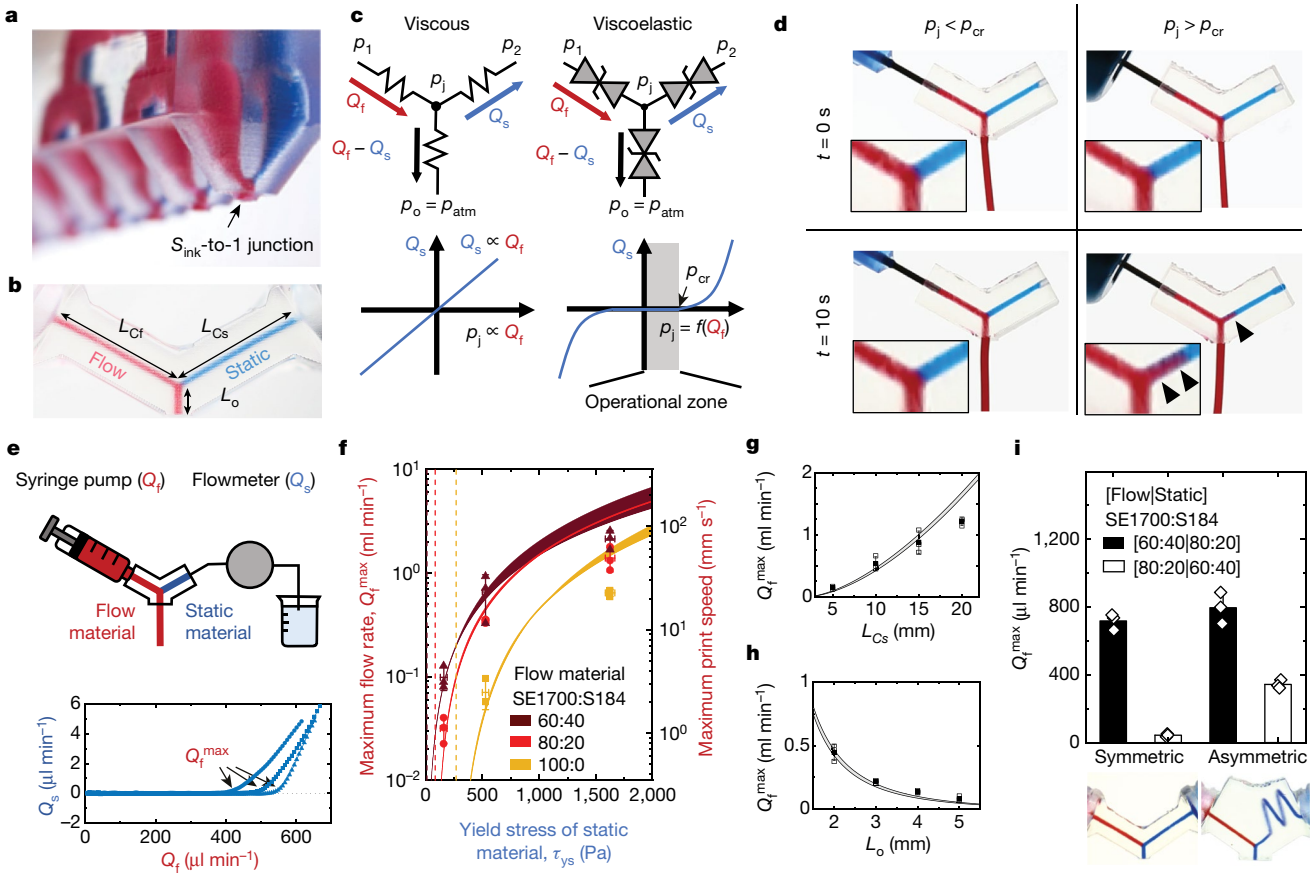

Fig. 2 | Viscoelastic ink flow through MM3D printheads. a, An 8 × 1 two-material MM3D printhead with S_{ink}-to-1 junctions (arrow). **b**, Simplified two-material nozzle with constant channel diameter, used for modelling viscoelastic flow behaviour. L_{Cf}, length of the flow-material channel; L_{Cs}, length of the static-material channel; L_o, length of the outlet channel. **c**, Circuit diagrams for viscous (left) and viscoelastic yield stress (right) materials at a Y-junction, and illustrative plots of the static flow Q_s versus the back-pressure generated at the junction, p_j. **d**, Time-lapse imaging of viscoelastic flow in a Y-junction at low (left) and high (right) extrusion rates. Arrowheads indicate the occurrence of backflow. **e**, Schematic showing the setup used for measuring the yielding of the static material under a ramping extrusion rate of the flow material (top) and representative plot of Q_s versus Q_f (bottom). **f**, Maximum flow rate, Q_f^{max}, for various flow materials when printed alongside various static materials. The materials are formulated from SE1700 and S184 silicones in weight ratios of 60:40, 80:20 and 100:0. Horizontal error bars denote the 95% confidence interval for the yield stress extracted from Extended Data Fig. 4c. Vertical error bars denote the standard deviation of the flow measurements from $n = 3$ experiments using separate nozzles. Dashed lines represent zeros from equation (14). **g**, **h**, Q_f^{max} increases with the length of the static-material channel, L_{Cs} (**g**), and decreases with the length of the outlet channel, L_o (**h**). Shaded curves in **f**–**h** represent the maximum and minimum bounds of the predicted values from equation (14), obtained using $n = 3$ measurements of the flow curves for each flow material. **i**, Q_f^{max} for two different inks in matched and unmatched nozzles. Error bars in **g**–**i** represent the standard deviation from $n = 3$ experiments using separate nozzles.

At material switch points, the 90–10% transition was measured at about 320 µm, which, at a print speed of 20 mm s^{-1}, represents a switch time of 16 ms and a characteristic switching frequency of about 60 Hz. Using data derived from a bitmap, large, periodic and complex patterns were rapidly produced with the parallel-print-path method using an 8 × 1 two-material printhead via MM3D printing (Fig. 3d, e, Supplementary Video 5). To demonstrate the island-printing method, we created continuous meandering shapes using an 8 × 1 four-material MM3D printhead (Fig. 3f, g, Supplementary Video 6). We note that MM3D printheads are capable of patterning a broad range of structural, functional and biological inks developed for DIW, including gelatin, which exhibits the requisite yielding behaviour for bioprinting[12,20,21,23] (Extended Data Fig. 8).

MM3D printing of functional objects

To demonstrate the ability to spatially program the composition, structure and properties of printed objects, we first fabricated a Miura origami pattern (Fig. 4a, b, Supplementary Video 7) using an 8 × 1 D MM3D printhead. This pattern, which is traditionally produced by folding paper, allows one to transform a sheet with a large surface area into a compact 3D structure[14,24]. Previous studies used laser cutting to generate multiple stacked layers, which are then manually assembled to create flexible and stiff regions[25–27]. Using MM3D printing, we generated Miura patterns rapidly in a single step by co-depositing two viscoelastic epoxy inks, which, when cured, exhibit different Young's moduli: 0.61 ± 0.16 MPa for the flexible hinges and 3.92 ± 0.40 GPa (mean ± s.d., $n = 5$) for the stiff origami faces (Fig. 4c, d). These hinges display a characteristic transition, from soft to stiff, over a distance of about 400 µm (Fig. 4e). Because reactive epoxy inks typically have short pot lives (Extended Data Fig. 9a–d), MM3D printing is well suited for fabricating these large-scale structures owing to the greatly reduced build times needed (Fig. 4f). The resulting Miura structure exhibits high deformability in the hinges and is capable of multiple folding cycles (1,632 ± 217; mean ± s.d., $n = 6$) before failing (Supplementary Video 7, Extended Data Fig 9e–g). Notably, failure typically occurs within the flexible hinge, away from the material transition zone.

To further highlight the capabilities of MM3D printing, we designed and fabricated a soft robot composed of rigid and soft elastomers patterned with millipede-like features, and embedded pneumatic actuators in modular form (Fig. 5a, Extended Data Fig. 10, Supplementary

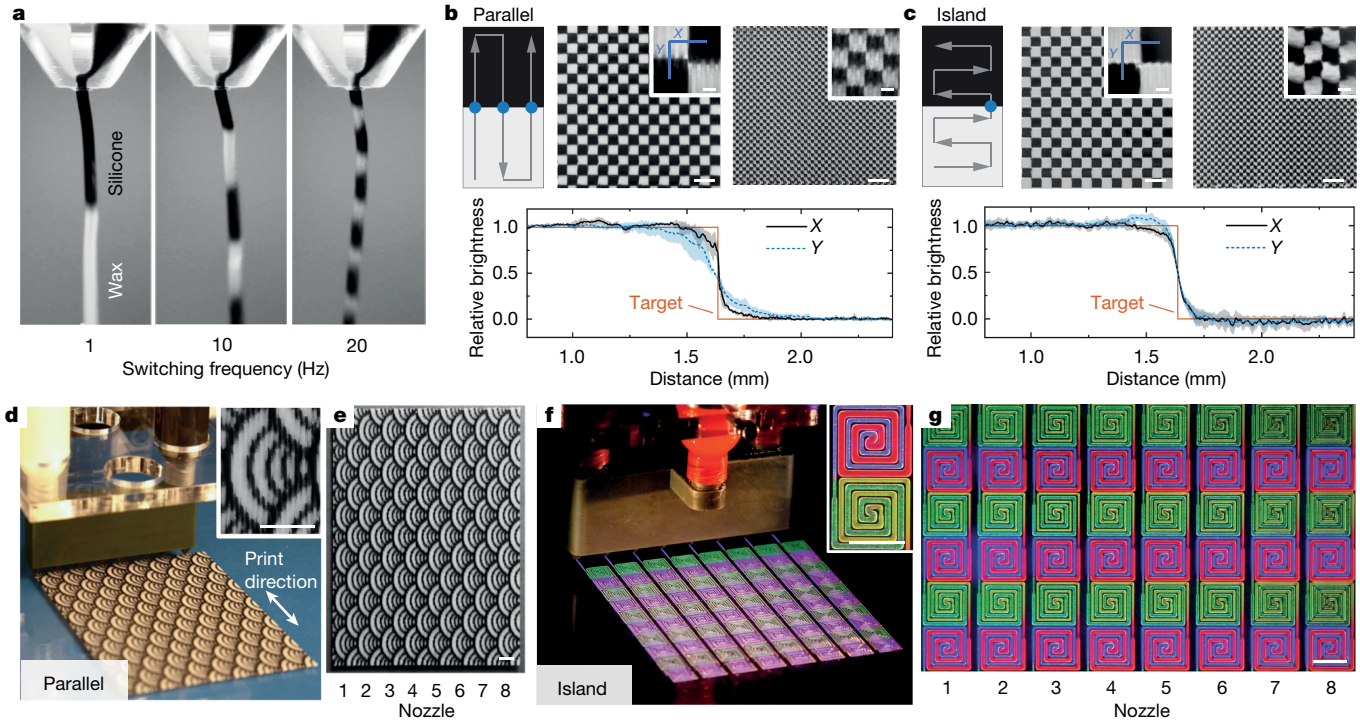

Fig. 3 | Printing voxelated matter. a, A two-material nozzle producing a single continuous voxelated filament at increasing switching frequencies. **b**, **c**, Chequerboard patterns of silicone (black) and wax (white) manufactured by an 8 × 1 MM3D printhead and the corresponding material transitions for the parallel (**b**) and island (**c**) methods of printing. Shaded regions represent the standard deviation from $n = 6$ measurements. Scale bars in **b**, **c**, 8 mm; scale bars in insets, 1 mm. The brightness values were normalized to the brightness of white and black regions far (> 1 mm) from the transition zones to derive the relative brightness. **d**, **e**, Parallel printing of an arbitrary pattern in silicone (black) and wax (white) using an asymmetric 8 × 1 two-material MM3D printhead. **f**, **g**, An 8 × 1 four-material MM3D printhead producing silicone spiral patterns by following a nonlinear island print path. Scale bars in **d**–**g**, 5 mm.

Video 8). Many soft robots rely on actuators arranged in periodic geometries, making them well suited to MM3D printing[28,29]. In our soft-robotic walkers, each millipede walker module is composed of 16 pneumatic actuators that are interconnected by a pair of underlying pneumatic networks, with one channel connecting the inner two columns of actuators and another channel connecting the outer two columns. When a vacuum is applied to these channels, the soft silicone 'muscle' buckles, causing a lateral and vertical displacement of the stiff 'leg' (ΔX and ΔY, respectively; Fig. 5b). To realize this design, we simultaneously printed both flexible (0.225 ± 0.005 MPa; mean ± s.d., $n = 5$; blue) and stiff (1.81 ± 0.05 MPa; mean ± s.d., $n = 5$; grey) silicone inks (Fig. 5c) in a motif that includes overhanging walls and spanning gaps that generate closed channels. To achieve a walking motion, the legs were actuated as shown in Fig. 5d, e, so that the ΔY displacement resulted in the weight of the soft robot resting on alternating actuator groups. The antisymmetric arrangement of the two sets of actuators ensured that the power strokes for each actuator group provided a lateral displacement ΔX in a consistent direction to achieve forward

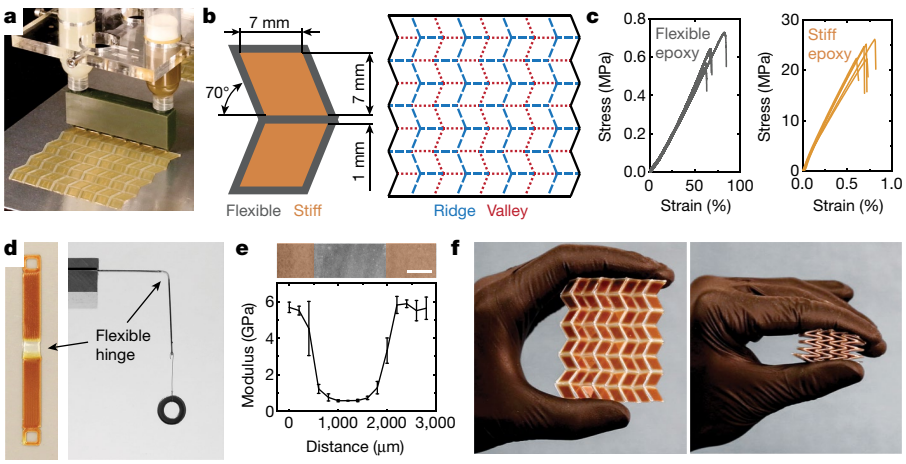

Fig. 4 | MM3D printing of origami structures. a, MM3D printing of a Miura pattern using an 8 × 1 two-material MM3D printhead. **b**, Design of a Miura folding pattern. **c**, Stress–strain curves from $n = 5$ tensile tests for flexible (0.61 ± 0.16 MPa; mean ± s.d.; grey) and stiff (3.92 ± 0.40 GPa; mean ± s.d.; orange) epoxies. **d**, Printed cantilevers (stiff; orange) and a hinge (flexible; grey) demonstrate patterned bending. **e**, Nanoindentation test of an interfacial region, measuring a transition length of about 400 μm (10% to 90%). Error bars represent the standard deviation from $n = 6$ measurements. Scale bar, 500 μm. **f**, Folding behaviour of an 8 × 8 Miura pattern. Print time, 2 min 30 s.

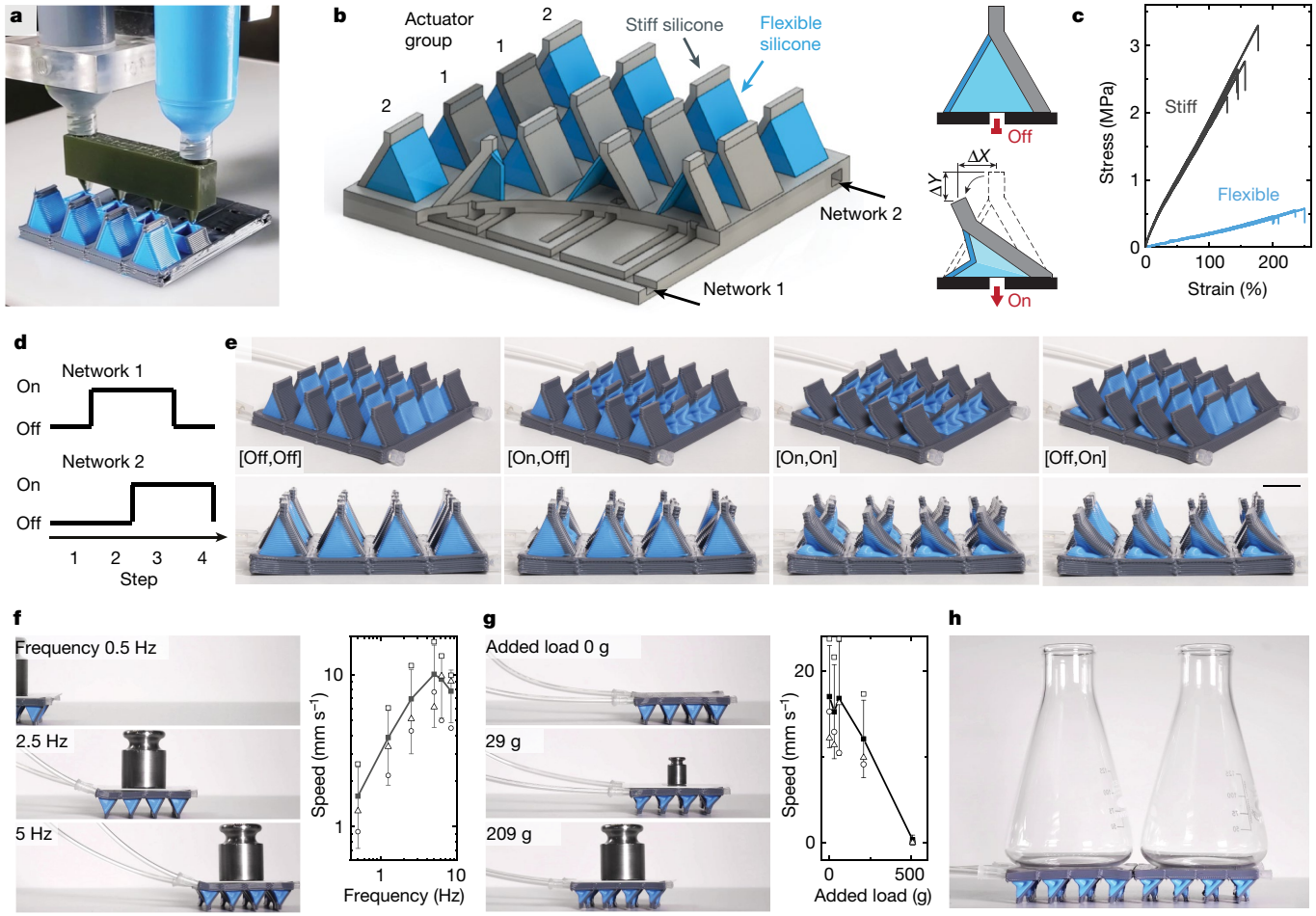

Fig. 5 | MM3D printing of soft-robotic walkers. a, MM3D printing of a soft robotic millipede walker using a 4 × 1 two-material MM3D printhead. Print time, 17 min. **b**, Illustration of the design elements of the walker. **c**, Stress–strain curves from $n = 5$ tensile tests for stiff (1.81 ± 0.05 MPa; mean ± s.d.; grey) and flexible (0.225 ± 0.005 MPa; mean ± s.d.; blue) silicones. **d**, Actuation pattern for the two channel networks used to produce locomotion. Four actuation steps comprise one cycle. **e**, Photographs of the four actuation states corresponding to the steps described in **d**, depicting the buckling of the flexible silicone 'muscles' and the displacement of the stiff silicone 'legs'. Scale bar, 10 mm. **f**, Walking speed of the soft robotic millipede as a function of cycle frequency. Added weight, 209 g. **g**, Walking speed of the soft-robotic millipede as a function of added weight. Cycle frequency, 5 Hz. Error bars in **f** and **g** represent the standard deviation of the speed measured for $n = 3$ independent walkers. **h**, A pair of soft robotic millipede modules connected in series to generate a longer walker, which is capable of transporting large labware.

locomotion. At its optimum cycling frequency of 5 Hz, the soft-robotic actuators (weighing about 25 g) could move at about 1 cm s^{-1} while carrying loads of up to about 200 g—that is, eight times their mass (Fig. 5f, g, Supplementary Video 9). Finally, two or more of these actuator modules can be connected in series to produce longer, millipede-like soft robots that carry greater loads (Fig. 5h, Supplementary Video 10).

Summary and conclusions

We present a powerful and versatile approach to generating voxelated soft matter using MM3D printing. By harnessing the pressure-driven flow behaviour of yield stress fluids, we seamlessly switch between multiple materials at high frequencies to enable continuous printing of heterogeneous voxelated filaments. By designing and implementing multimaterial multinozzle printheads, we rapidly construct 3D objects with spatially programmed composition, structure and properties. While two embodiments—namely, foldable origami patterns and soft robots that locomote—are printed to highlight these capabilities, a broad range of high-performance structural, functional and biological materials can be patterned by MM3D printing. Moving forward, the next generation of MM3D printheads would ideally feature independently addressable nozzles with smaller diameters arranged in even larger arrays. These improvements would eliminate the periodicity constraints imposed by the current printhead design while simultaneously leading to improved feature resolution and lower build times. Ultimately, we envision creating 3D voxelated matter on demand with superior performance via the close coupling of MM3D printing, predictive design and optimization.

Online content

Any methods, additional references, Nature Research reporting summaries, source data, extended data, supplementary information, acknowledgements, peer review information; details of author contributions and competing interests; and statements of data and code availability are available at https://doi.org/10.1038/s41586-019-1736-8.

1. Hosny, A. et al. From improved diagnostics to presurgical planning: high-resolution functionally graded multimaterial 3D printing of biomedical tomographic data sets. *3D Print. Addit. Manuf.* **5**, 103–113 (2018).
2. Bader, C. et al. Making data matter: voxel printing for the digital fabrication of data across scales and domains. *Sci. Adv.* **4**, eaas8652 (2018).
3. Gu, G. X., Chen, C. T., Richmond, D. J. & Buehler, M. J. Bioinspired hierarchical composite design using machine learning: simulation, additive manufacturing, and experiment. *Mater. Horiz.* **5**, 939–945 (2018).

4. Gu, G. X., Chen, C. T. & Buehler, M. J. De novo composite design based on machine learning algorithm. *Extreme Mech. Lett.* **18**, 19–28 (2018).
5. Jang, D., Kim, D. & Moon, J. Influence of fluid physical properties on ink-jet printability. *Langmuir* **25**, 2629–2635 (2009).
6. Truby, R. L. & Lewis, J. A. Printing soft matter in three dimensions. *Nature* **540**, 371–378 (2016).
7. Raney, J. R. et al. Rotational 3D printing of damage-tolerant composites with programmable mechanics. *Proc. Natl Acad. Sci. USA* **115**, 1198–1203 (2018).
8. Wehner, M. et al. An integrated design and fabrication strategy for entirely soft, autonomous robots. *Nature* **536**, 451–455 (2016).
9. Valentine, A. D. et al. Hybrid 3D printing of soft electronics. *Adv. Mater.* **29**, 1703817 (2017).
10. Kotikian, A., Truby, R. L., Boley, J. W., White, T. J. & Lewis, J. A. 3D printing of liquid crystal elastomeric actuators with spatially programed nematic order. *Adv. Mater.* **30**, 1706164 (2018).
11. Kong, Y. L. et al. 3D printed quantum dot light-emitting diodes. *Nano Lett.* **14**, 7017–7023 (2014).
12. Kolesky, D. B., Homan, K. A., Skylar-Scott, M. A. & Lewis, J. A. Three-dimensional bioprinting of thick vascularized tissues. *Proc. Natl Acad. Sci. USA* **113**, 3179–3184 (2016).
13. Compton, B. G. & Lewis, J. A. 3D-printing of lightweight cellular composites. *Adv. Mater.* **26**, 5930–5935 (2014).
14. Schenk, M. & Guest, S. D. Geometry of Miura-folded metamaterials. *Proc. Natl Acad. Sci. USA* **110**, 3276–3281 (2013).
15. Bendsøe, M. P. & Sigmund, O. Material interpolation schemes in topology optimization. *Arch. Appl. Mech.* **69**, 635–654 (1999).
16. Haftka, R. T. & Gürdal, Z. *Elements of Structural Optimization* (Springer Science & Business Media, 2012).
17. Ober, T. J., Foresti, D. & Lewis, J. A. Active mixing of complex fluids at the microscale. *Proc. Natl Acad. Sci. USA* **112**, 12293–12298 (2015).
18. Kokkinis, D., Bouville, F. & Studart, A. R. 3D printing of materials with tunable failure via bioinspired mechanical gradients. *Adv. Mater.* **30**, 1705808 (2018).
19. Hardin, J. O., Ober, T. J., Valentine, A. D. & Lewis, J. A. Microfluidic printheads for multimaterial 3D printing of viscoelastic inks. *Adv. Mater.* **27**, 3279–3284 (2015).
20. Liu, W. et al. Rapid continuous multimaterial extrusion bioprinting. *Adv. Mater.* **29**, 1604630 (2017).
21. Kolesky, D. B. et al. 3D bioprinting of vascularized, heterogeneous cell-laden tissue constructs. *Adv. Mater.* **26**, 3124–3130 (2014).
22. Hansen, C. J. et al. High-throughput printing via microvascular multinozzle arrays. *Adv. Mater.* **25**, 96–102 (2013).
23. Skylar-Scott, M. A. et al. Biomanufacturing of organ-specific tissues with high cellular density and embedded vascular channels. *Sci. Adv.* **5**, eaaw2459 (2019).
24. Miura, K. The science of Miura-ori: a review. In *4th International Meeting of Origami Science, Mathematics, and Education* (ed. Lang, R. J.) 87–100 (CRC Press, 2009).
25. Overvelde, J. T. B., Weaver, J. C., Hoberman, C. & Bertoldi, K. Rational design of reconfigurable prismatic architected materials. *Nature* **541**, 347–352 (2017).
26. Babaee, S., Overvelde, J. T. B., Chen, E. R., Tournat, V. & Bertoldi, K. Reconfigurable origami-inspired acoustic waveguides. *Sci. Adv.* **2**, e1601019 (2016).
27. Boatti, E., Vasios, N. & Bertoldi, K. Origami metamaterials for tunable thermal expansion. *Adv. Mater.* **29**, 1700360 (2017).
28. Bartlett, N. W. et al. A 3D-printed, functionally graded soft robot powered by combustion. *Science* **349**, 161–165 (2015).
29. Polygerinos, P. et al. Soft robotics: review of fluid-driven intrinsically soft devices; manufacturing, sensing, control, and applications in human-robot interaction. *Adv. Eng. Mater.* **19**, 1700016 (2017).

Methods

Materials

Silicone inks with different shear yield stresses were prepared by centrifugal mixing (2,000 rpm, 2 min; Flak-Tek) of varying ratios of SE 1700 to Sylgard 184 (S184; Dow Corning). Their colour was modified by adding either 2% w/w pigment (Silc-Pig, Smooth-On) or 0.2% w/w fluorescent dye (Risk Reactor). Wax inks were prepared by mixing microcrystalline wax (SP-19, Strahl & Pitsch) with petroleum jelly (Unilever) at a 4:6 weight ratio. The wax and petroleum jelly were combined in a covered glass beaker and heated in a furnace to 100 °C until melted (about 2 h), followed by stirring and filtering through a 2-μm-pore-diameter glass fibre syringe filter (Millex AP 20, MilliporeSigma). The wax ink was stored at room temperature for less than one month in a covered container. Immediately before use, the wax was mixed with 2% w/w pigment (Silc-Pig) in a centrifugal mixer (2,000 rpm, 2 min). The flexible epoxy ink was prepared by mixing batches of 30 g of Epon 8130 (Momentive Performance Materials) with 4.5 g of CAB-O-SIL TS-530 fumed silica (Cabot Corporation), which was added in stepwise increments of 1.5 g to 'max 100' containers (FlakTek Ink). The solution was mixed in a DAC 600 VAC speed mixer (FlackTek) in vacuum (20 torr) after each step (90 s at 800 rpm, 90 s at 1,600 rpm and 120 s at 2,000 rpm). After allowing the inks to cool to room temperature, 3 g of Epikure 3272 curing agent (Hexion) was added and mixed for 30 s at 800 rpm, 30 s at 1,600 rpm and 60 s at 2,000 rpm. Similarly, the stiff epoxy ink was prepared by mixing 30 g of Epon 826 (Momentive Performance Materials) with 9 g nanoclay platelets (Nanocar 1.34 TN, Southern Clay Products) in stepwise increments of 3 g and 2.1 g dimethyl methyl phosphonate (Sigma Aldrich). 1.5 g of Basionics VS03 curing agent (BASF) was added after the ink reached room temperature and was mixed in the speed mixer accordingly. The same mixing cycles as those used for the flexible ink were used. For the soft robots, the stiff silicone ink was prepared by combining SE 1700 base and catalyst at a 10:1 weight ratio and then by adding 2% w/w pigment (Silc-Pig) in a centrifugal mixer (2,000 rpm, 2 min). The flexible silicone ink was prepared by first mixing SE 1700 base (40 g), catalyst (1.6 g) and pigments (1 g) in a speed mixer (2,000 rpm, 2 min), followed by adding Sylgard 527 Part A (3.4 g) and Part B (3.4 g) and mixing again (2,000 rpm, 2 min).

Gelatin inks, 15% w/v, were prepared by stirring gelatin (type A; 300 bloom from porcine skin; Sigma) with phosphate buffered saline (PBS) without calcium or magnesium in a covered Erlenmeyer flask, at 85 °C for 12 h. The molten gelatin was then brought to pH 7.5 by dropwise addition of 1 M NaOH and filtered using a 0.2-μm vacuum filter. The molten gelatin was then diluted in PBS to 7.5% w/v and coloured by addition of 1% v/v food colouring. The molten gelatin was directly pipetted into a syringe, covered and allowed to undergo gelation by incubating at 4 °C. Kept sterile, the syringe could be stored for up to six months at 4 °C.

MM3D printheads

The MM3D printheads were designed using 3D computer-aided design software (SolidWorks). The model was converted to a stereolithography (.stl) file and printed using a stereolithography 3D printer (Perfactory Aureus, Envisiontec). For all high-resolution MM3D printheads, HTM140_v2 green resin was used, with a layer height of 50 μm and a calibrated power of 600 mW. Alternatively, for visualization purposes, clear resin (EShell 300) was used with a layer height of 100 μm and a calibrated power of 120 mW. Once printed, the nozzles were rinsed with isopropyl alcohol using a syringe to flush the channels. The nozzles were then dried under a stream of air and stored in the dark until they were ready for use.

The MM3D printheads were attached to a set of ink-filled syringes that were mounted on a six-axis air-bearing linear-motion controller described previously[21]. Pressure was supplied to the syringes via digital pressure regulators (Ultimus V, Nordson EFD) that were gated through pneumatic solenoid valves (VQD1151, SMC). The solenoid valves were operated by 0–24-V digital relays (WAGO) that were synchronized to the print motion through an NPAC A3200 motion controller (Aerotech).

Rheological measurements

The ink rheology was determined using a controlled stress rheometer (TA Instruments) with a cone–plate geometry with a diameter of 40 mm and a cone angle of 2°. After inks were loaded into the cone–plate gap, excess ink was removed using a spatula. Apparent viscosities were determined at 20 °C by carrying out shear-rate sweeps using shear rates of about 1 s^{-1} to about 100 s^{-1}. The data were fitted using a Herschel–Bulkley model to determine the consistency, flow index and shear yield stress for each ink. The storage and loss moduli of the epoxy inks were measured at oscillation frequencies from 0.1 Hz to 10 Hz by applying a shear stress of 10 Pa. Next, oscillatory amplitude sweeps were performed using strains of 0.01% to 1,000% at a frequency of 1 Hz. The experiments were conducted within 30 min of preparing the inks. To assess the ink pot life, the complex viscosity was measured for 15 h at 1% strain applied at a frequency of 2 Hz.

To measure static yield stresses, silicone inks of various compositions were loaded into metal tubing with inner diameter of 0.84 mm and length ranging from 12.35 mm to 44.10 mm. A pressure controller (Ultimus V, Nordson EFD) was connected in series with a microfluidic flowmeter (GeSiM) via water-filled tubing. The applied pressure was increased stepwise, and yielding was determined to occur at the onset of flow ($Q_s > 0.1$ μl min^{-1}). This yield pressure was measured for each tube length, and the gradient of the line was used to calculate the static shear yield stress of the ink. To measure Q_f^{max} for different combinations of static and flow materials, a gas-tight glass syringe (Hamilton) was loaded with a silicone ink via centrifugation and was mounted onto a syringe pump. Care was taken to avoid introducing air bubbles upon insertion of the plunger. The 'flow' side of a model MM3D nozzle was connected to the syringe, while the 'static' side of the printhead, loaded with a second silicone ink, was connected via water-filled tubing to the microfluidic flowmeter. The flow rate was ramped stepwise until an onset of flow ($Q_s > 0.1$ μl min^{-1}) was detected by the microfluidic flowmeter, at which point the static material was deemed to have yielded.

Printing voxelated matter

Both Muira origami patterns and 3D voxelated architectures were fabricated on a stage (Aerotech) fitted with EFD Ultimus V pressure regulators (Nordson). Five or more dogbone and hinge specimens were printed onto glass slides with a single two-material switching nozzle at a print speed of 8 mm s^{-1} and pressures of 51 psi and 59 psi (1 psi = 6,895 N m^{-2}) for the flexible and stiff inks, respectively. The Miura patterns were printed with a print speed of 10 mm s^{-1} and pressures of 55 psi and 66 psi for the flexible and stiff inks, respectively. The soft robots were printed with a print speed of 40 mm s^{-1} and the flexible and stiff silicones were printed at pressures of 53 psi and 62 psi, respectively. The samples were cured in a furnace for 18 h at a constant temperature of 100 °C with no ramping up or down. The dogbone specimen tests were conducted according to ASTM D638-10 on an Instron 5566 Universal Testing Machine fitted with pneumatic grippers mounted on static load cells of 100 N and 1,000 N (depending on the maximum required load) at a testing speed of 10 mm s^{-1} (Instron). On the same machine, cyclic tests were conducted at a frequency of 6 Hz with an amplitude resulting in an angular displacement ranging from 18° to 142° (Extended Data Fig. 9e, f). The soft robots were actuated using a vacuum pressure that was gated via a pair of pneumatic solenoid valves (VQD1151, SMC). The solenoid valves were controlled as described for the operation of the MM3D printheads. To measure the walking speed, videos were analysed for three different soft-robotic millipedes to estimate the time required for each to move by one body length. The printer motion was controlled via GCode, which was either coded manually or, for more complex print patterns, generated automatically from bitmap files using a custom script (MATLAB, Mathworks). Bitmaps were designed

manually or could be generated from a .stl file using Freesteel Slicer. The custom MATLAB script read the bitmap file and generated a bidirectional parallel-rastering print path while simultaneously switching material on the fly to produce the pattern. The exact switching location was controlled by an offset variable, which was tuned by bidirectionally printing vertical lines to visualize the alignment. The 2D MM3D printheads were physically aligned to the print substrates (glass slides) using a two-axis tilt stage.

Scaling laws for MM3D printing

We consider an MM3D printhead that is extruding filaments with diameter D, is translating at a print speed v and is switching materials at a switching frequency f (Extended Data Fig. 3). The resulting voxels are roughly cylindrical, with diameter D and an axial length given by:

$$l_v = \frac{v}{f} \tag{1}$$

The nozzle has a maximum switching frequency of f_{max}, which is limited by the cycling time of the pneumatic solenoids and the resistance and capacitance of the air channels and syringe. If the nozzle operates at its maximum switching frequency and the print speed is set such that $v = Df_{max}$, then the cylindrical voxels become roughly cubic, that is, $l_v = D$. The characteristic build time (t) required to print an arbitrary voxelated part of characteristic length L using an array of N nozzles is given by:

$$t \approx \frac{L^3}{D^2 v N} = \frac{L^3}{D^3 f_{max} N} \tag{2}$$

Here, the cubic dependency on the part size can be ameliorated by using a printhead that is scaled with part size, that is:

$$N = \left(\frac{L}{l}\right)^k \tag{3}$$

where l is the spacing between nozzles and $k \in \{0, 1, 2\}$ represents the dimensionality of the nozzle array. Given these parameters, we can vastly reduce the total build time from $O(L^3)$ for a single nozzle to $O(L^2)$ for a 1D nozzle array or to $O(L)$ for a 2D nozzle array (Fig. 1a):

$$t \approx \frac{L^{3-k} l^k}{D^2 v} \tag{4}$$

By decreasing the distance between individual nozzles within the printheads—that is, the nozzle spacing parameter l—we can reduce the build time required for a given 3D object. However, if each nozzle is restricted to printing the same material at any given time, the part complexity is decreased owing to periodicity constraints; that is, as the spacing is decreased, less information can be encoded within the printed object (Extended Data Fig. 3). Specifically, the number of bits of information that can be encoded into a cube of side length L by a nozzle printing at speed v that can switch between S_{ink} materials (where S_{ink} is the number of ink-filled syringes attached to the MM3D printhead) at a maximum frequency of f_{max} is given by:

$$I = \frac{L^{3-k} l^k}{D^2 v} f_{max} \log_2 S_{ink} = t f_{max} \log_2 S_{ink} \tag{5}$$

Importantly, this analysis suggests that implementation of MM3D printheads with high S_{ink}, N and f_{max} would enable the rapid construction of complex 3D architectures with a minimum voxel size approaching D^3.

Analytical model for viscoelastic inks at a junction

We consider the force balance for a static plug of complex fluid in a cylindrical channel. The critical pressure p_{cr} at which the plug will yield is given by:

$$p_{cr} = \frac{4\tau_{ys} L_{Cs}}{d} \tag{6}$$

where $\tau_{ys} \in \{\tau_{y1}, \tau_{y2}\}$ is the shear yield stress of the static material and $L_{Cs} \in \{L_{C1}, L_{C2}\}$ and d are the length and diameter of the static channel, respectively[30]. We note that upon toggling the actuation states of the pneumatic solenoid valves, the material in the static channel begins to flow under pressure, whereas the previously flowing material now becomes static. In addition, a compensatory forward pressure ($p_s > p_{atm}$) could be applied to the inlet of the static side to resist yielding at a higher p_j, in which case backflow is prevented when:

$$p_j - p_s < p_{cr} \tag{7}$$

The junction back pressure, p_j, results from the flow of the flow material, Q_f. For a Herschel–Bulkley material flowing through a cylindrical pipe, Chilton & Stainsby[30] provide the following closed-form solution:

$$p_j = \frac{4k_f L_o}{d}\left(\frac{8V_f}{d}\right)^{n_f}\left(\frac{3n_f+1}{4n_f}\right)^{n_f}\left(\frac{1}{1-X}\right)\left(\frac{1}{1-aX-bX^2-cX^3}\right)^{n_f} \tag{8}$$

where:

$$a = \frac{1}{2n_f+1} \tag{9}$$

$$b = \frac{2n_f}{(n_f+1)(2n_f+1)} \tag{10}$$

$$c = \frac{2n_f^2}{(n_f+1)(2n_f+1)} \tag{11}$$

$$X = \frac{4L_o\tau_{yf}}{dp_j} \tag{12}$$

and k_f, n_f and τ_{yf} are the Herschel–Bulkley consistency index, the flow index and the shear yield stress, respectively, for the flowing material, and L_o is the outlet channel length. To solve for p_j for a given mean velocity V_f, this implicit equation requires an iterative solution. However, for a given p_j, we can rearrange this equation to provide an explicit solution for V_f:

$$V_f = \frac{d}{8}\left[\frac{dp_j}{4k_f L_o}\left(\frac{4n_f}{3n_f+1}\right)^{n_f}(1-X)(1-aX-bX^2-cX^3)^{n_f}\right]^{\frac{1}{n_f}} \tag{13}$$

At the critical mean velocity, V_{cr}, the junction pressure is sufficient to cause yielding of the static material: $p_j = p_{cr}$ (assuming $p_s = p_{atm}$). By substituting p_j in equation (12) and equation (13) for p_{cr} in equation (6), we derive an explicit solution for V_{cr}:

$$V_{cr} = \frac{d}{8}\left[\frac{\tau_{ys} L_{Cs}}{k_f L_o}\left(\frac{4n_f}{3n_f+1}\right)^{n_f}(1-X_{cr})(1-aX_{cr}-bX_{cr}^2-cX_{cr}^3)^{n_f}\right]^{\frac{1}{n_f}} \tag{14}$$

where:

$$X_{cr} = \frac{4L_o\tau_{yf}}{dp_{cr}} = \frac{4dL_o\tau_{yf}}{4dL_s\tau_{ys}} = \frac{L_o\tau_{yf}}{L_{Cs}\tau_{ys}} \tag{15}$$

This critical print speed of the flow material can be related to the maximum volumetric extrusion rate by:

$$Q_f^{max} = \frac{\pi d^2}{4} V_{cr} \tag{16}$$

Equation (14) predicts a zero at $X_{cr} = 1$, where the static material yields with any non-zero flow rate of the flow material. These zeroes are shown as dotted lines for various selections of flow materials in Fig. 2f. The constraint $X_{cr} < 1$ results in a necessary geometric and material

design criterion that must be obeyed for all combinations of flow and static materials for the successful operation of an MM3D printhead (assuming a constant channel diameter):

$$\frac{\tau_{yf}}{\tau_{ys}} < \frac{L_{Cs}}{L_o} \tag{17}$$

Importantly, equation (17) shows that non-yield stress materials—that is, $\tau_{ys} = 0$—cannot be used in a pressure-driven MM3D system.

In general, the maximum constant print speed, v_{cr}, for MM3D printing of a set of materials, M, where $M = \{(\tau_{y,1}, n_1, k_1), \ldots, (\tau_{y,S_{ink}}, n_{S_{ink}}, k_{S_{ink}})\}$ is given by the minimum V_{cr} for all potential selections of flow materials ($f_m \in M$) and static materials ($s_m \in M$):

$$v_{cr} = \min_{f_m \in M,\, s_m \in M} V_{cr}(f_m, s_m) \tag{18}$$

Given that such materials may exhibit a wide range of flow behaviour, this could lead to a 'weakest-link' material that limits the print speed. Although v_{cr} can be made arbitrarily large by making $L_{C1} \ldots L_{CS_{ink}} \to \infty$ (assuming non-zero shear yield stresses), this would result in prohibitively high resistances to flow because viscoelastic DIW inks typically require high printing pressures (often much higher than 100 psi).

Data availability

The datasets generated or analysed during the current study are available from the corresponding author on reasonable request.

Code availability

The code generated during the current study is available from the corresponding author on reasonable request.

30. Chilton, R. A. & Stainsby, R. Pressure loss equations for laminar and turbulent non-Newtonian pipe flow. *J. Hydraul. Eng.* **124**, 522–529 (1998).

Acknowledgements We thank K. Bertoldi for discussions on origami. We also thank L. Sugita for experimental assistance; J. C. Weaver and L. K. Sanders for assistance with imaging, photography and videography; and T. Busbee for silicone ink formulations. This work was supported by the Vannevar Bush Faculty Fellowship Program, sponsored by the Basic Research Office of the Assistant Secretary of Defense for Research and Engineering through the Office of Naval Research Grant N00014-16-1-2823, the Harvard MRSEC (grant number DMR-1420570) and by GETTYLAB.

Author contributions M.A.S.-S., J.M. and J.A.L. conceived the project. M.A.S.-S. and J.M. designed the experiments. M.A.S.-S., J.M. and C.W.V. conducted the experiments and analysed the data. M.A.S.-S., J.M. and J.A.L. prepared the manuscript.

Competing interests J.A.L. is a co-founder of Voxel8, Inc. and M.A.S.-S. owns stock in Formlabs. A US patent has been filed by Harvard University on this research (application number 16/081,812).

Additional information
Supplementary information is available for this paper at https://doi.org/10.1038/s41586-019-1736-8.
Correspondence and requests for materials should be addressed to J.A.L.
Peer review information *Nature* thanks Yong Lin Kong, Eujin Pei and the other, anonymous, reviewer(s) for their contribution to the peer review of this work.
Reprints and permissions information is available at http://www.nature.com/reprints.

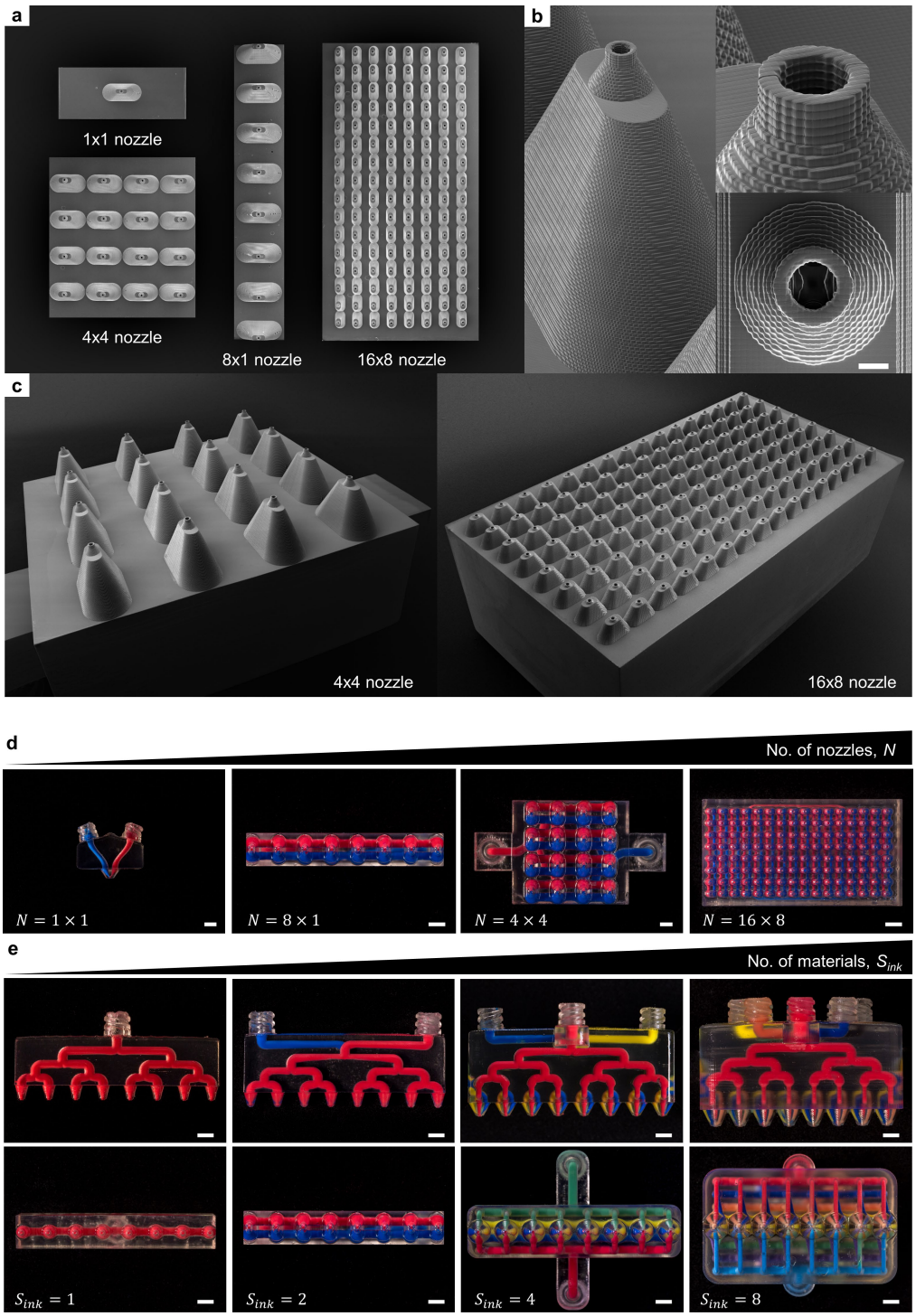

Extended Data Fig. 1 | Scanning electron microscope (SEM) images and photographs of MM3D printheads with varying numbers of nozzles and materials. a, SEM images (top–down view) of 0D (1 × 1), 1D (8 × 1) and 2D (4 × 4; 16 × 8) nozzle arrays for two-material MM3D printing. **b**, Higher-magnification SEM images of these printheads, showing an individual nozzle outlet (tilted and top–down views). Scale bar, 200 µm. **c**, SEM images (tilted views) of 4 × 4 and 16 × 8 two-material MM3D printheads. **d**, Photographs of MM3D printheads showing $N = 1 \times 1$, 8×1, 4×4 and 16×8 designs, which increase from 1 to 128 nozzles per printhead (from left to right), where $S_{ink} = 2$. **e**, Photographs showing side (top row) and top (bottom row) views of MM3D printheads with an increasing number of materials being delivered to each nozzle, where $N = 8 \times 1$. Scale bars, 5 mm.

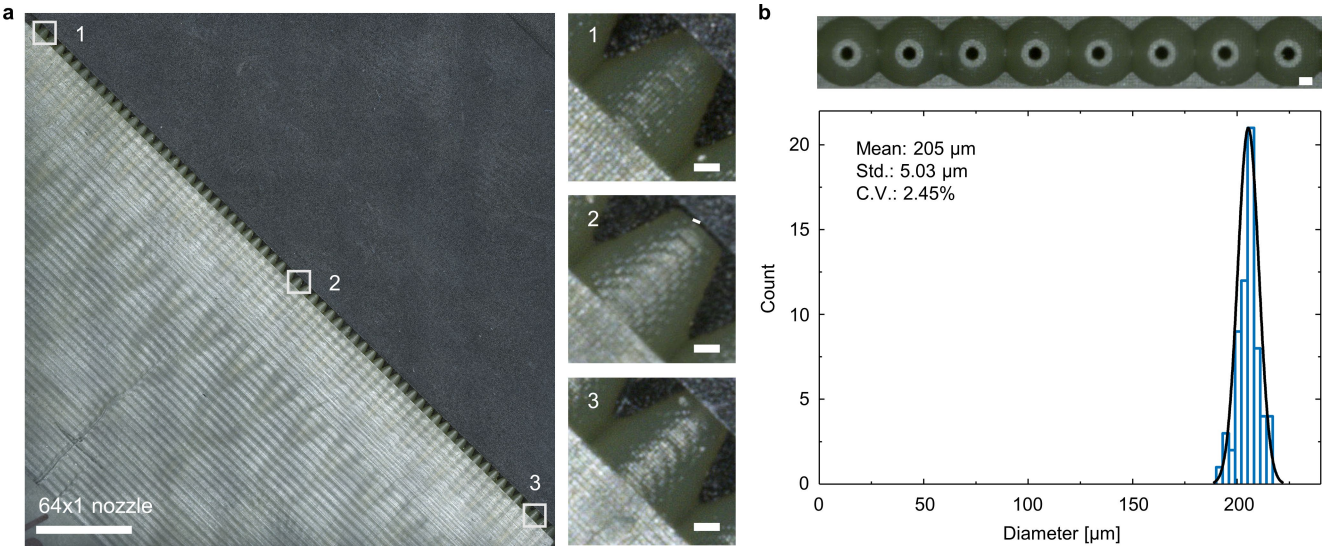

Extended Data Fig. 2 | Printhead flatness and hole diameter repeatability. **a**, 64 × 1 MM3D printhead fabricated using stereolithography. The printhead has a flatness of 8 µm across the total length of the nozzle (60 mm). Scale bars: left, 8 mm; right, 200 µm. **b**, Histogram showing the diameter of the nozzle outlets. The actual diameters of the nozzle outlets (diameter, 205 ± 5.03 µm; mean ± s.d.) are slightly larger than their designed diameter of 200 µm. (We note that the top image represents a representative view of eight nozzle outlets out of a total of 64 in this 1D nozzle array). Scale bar, 200 µm. Std, standard deviation; C.V., coefficient of variation.

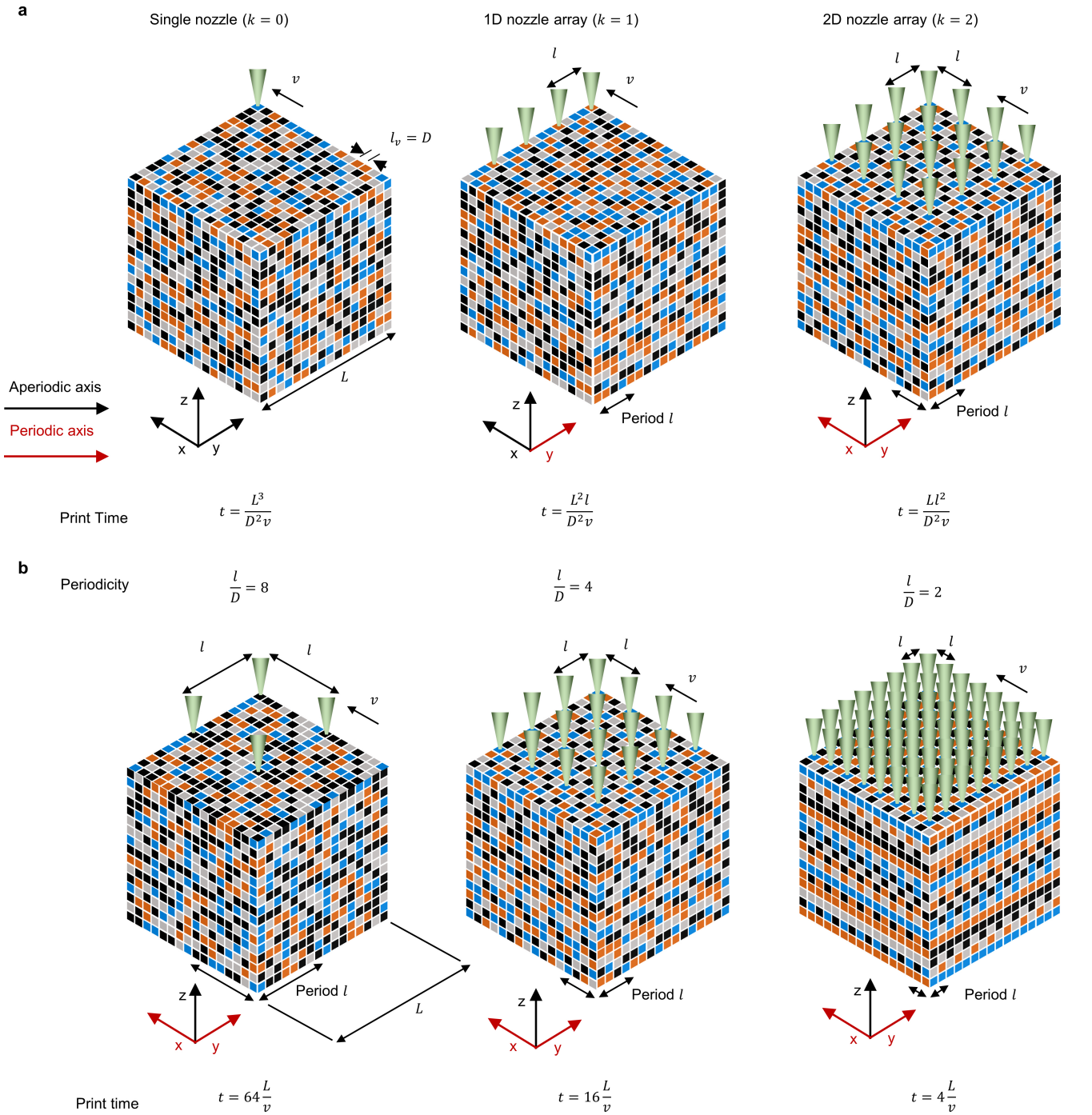

Extended Data Fig. 3 | Scaling laws for MM3D printing. a, The periodicity and print time depend on the dimensionality, k, of the MM3D printhead. A single nozzle (0D; left) has no periodic axis, providing the greatest complexity but longest print time. A 1D nozzle array is constrained to be periodic in one axis but reduces the print time from $O(L^3)$ to $O(L^2)$. The 2D nozzle array is periodic in two axes but results in the shortest print time of $O(L)$. **b**, The complexity and print time also depend on the spacing between nozzles in each printhead design. L, part length; D, nozzle diameter; l_v, voxel length; v, print speed; t, print time; l, nozzle spacing.

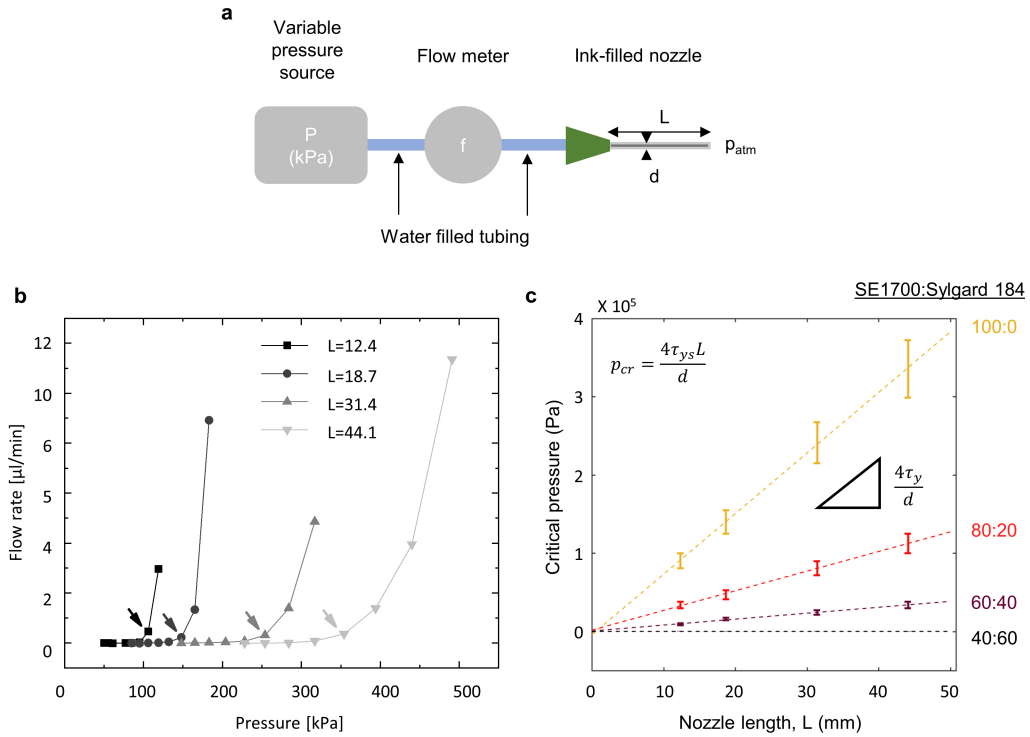

Extended Data Fig. 4 | Measurements of critical pressure, p_{cr}, for various nozzle lengths and materials. a, A variable pressure (P) source is placed in series with a microfluidic flowmeter and an ink-filled nozzle to measure the critical pressure for a given nozzle tip length, L. **b**, Representative set of measurements of flow rate versus pressure. The arrows represent the critical pressure for each nozzle tip length, at which yielding is first observed. **c**, Measured critical pressures analysed for different silicone elastomer inks (varying ratios of SE1700 to Sylgard 184) as a function of the nozzle length. The dashed lines are linear regression fits and error bars represent the resolution of the pressure steps used for the analysis ($n = 1$).

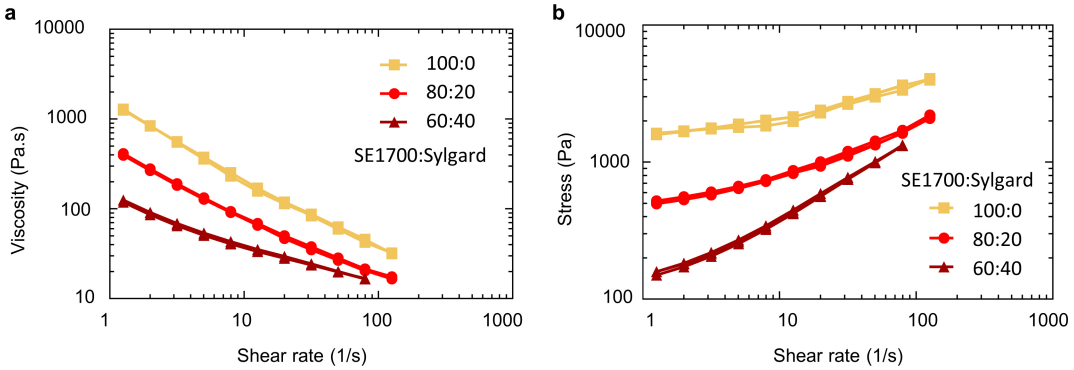

Extended Data Fig. 5 | Rheological properties of different silicone inks. **a**, **b**, Log–log plots of the apparent viscosity (**a**) and the shear stress (**b**) as a function of shear rate for silicone elastomer inks with different compositions (that is, different ratios of SE1700 to S184), fitted by the Herschel–Bulkley model. The data are from $n = 3$ independent experiments per ink.

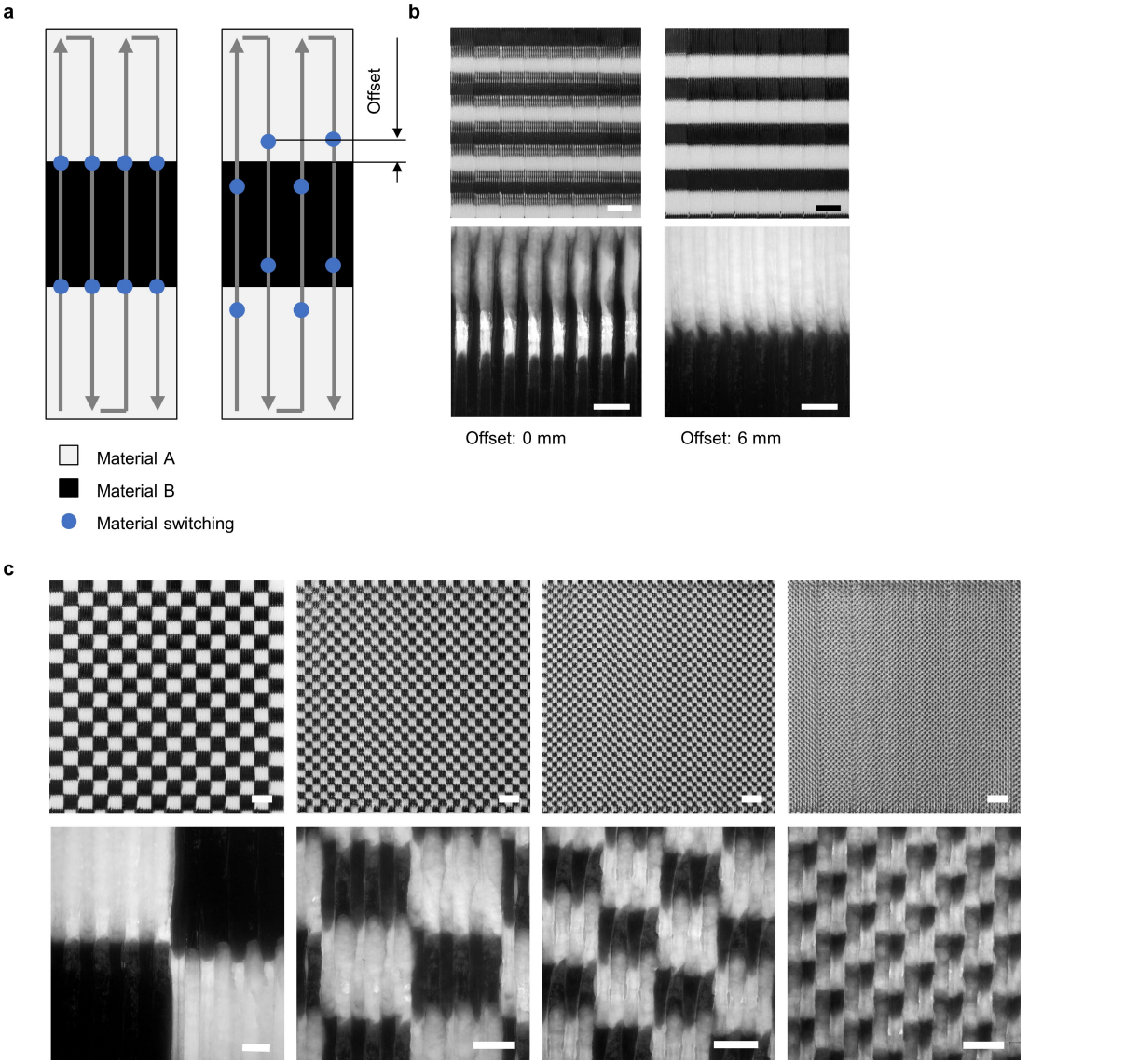

Extended Data Fig. 6 | Offset length and print-path design. a, **b**, Because of the finite output channel length, L_o, and inertance in the system, a delay occurs when switching between materials. This delay can be corrected by introducing an offset length (**a**) and during parallel printing of horizontal lines in silicone (black) and wax (white) (**b**). Scale bars: bottom, 1 mm; top, 8 mm. **c**, Offset-corrected printing of resolution grids using silicone and wax inks, showing increasingly smaller features (from left to right) and thus high switching frequencies. Scale bars: bottom, 1 mm; top, 5 mm.

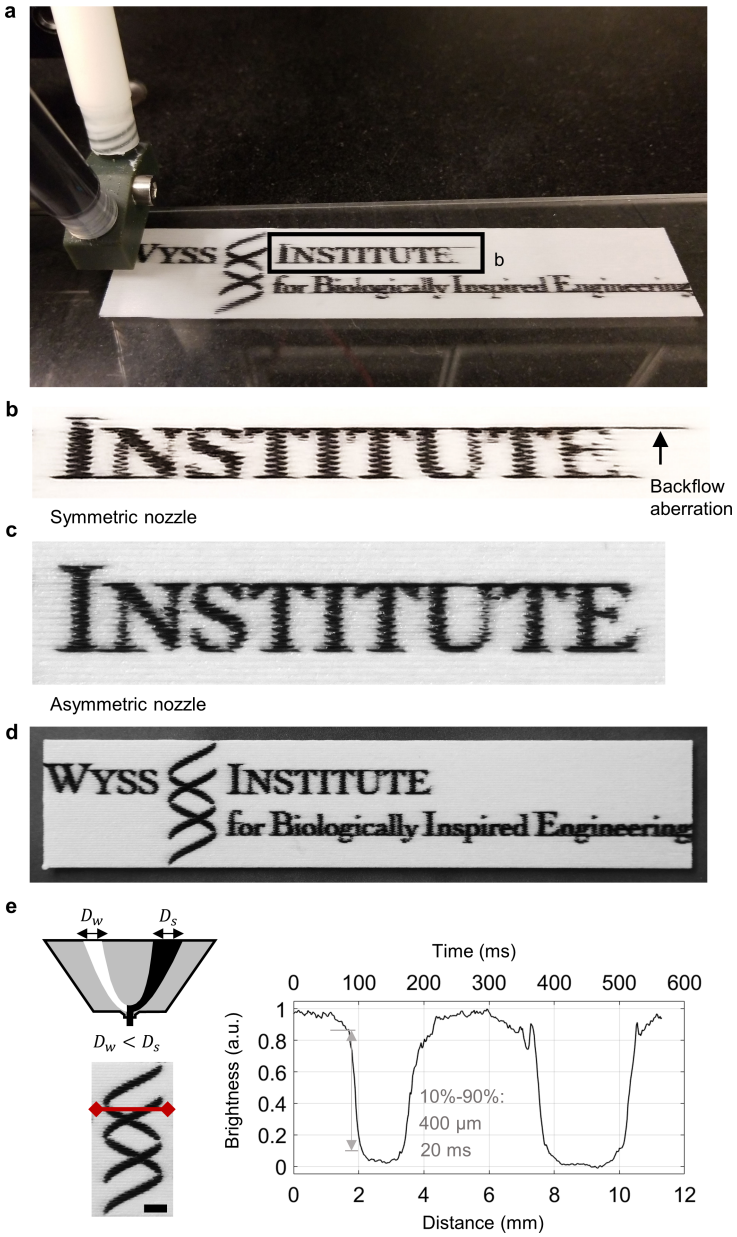

Extended Data Fig. 7 | Backflow aberration correction using an asymmetric nozzle. a, **b**, Printing a two-material pattern with a symmetric OD nozzle that switches between two materials (**a**) induces backflow aberrations (**b**) due to printhead operation at $v > V_{cr}$ for the silicone (black). The aberration occurs because of backflow of the stiffer black silicone into the channel with the softer white wax. Hence, after a long period of extruding black ink, undesired black ink flows out upon switching to the wax channel. **c**–**e**, An asymmetric nozzle in which the wax channel is narrower than the silicone channel prevents the occurrence of backflow aberrations. Scale bar in e, 4 mm.

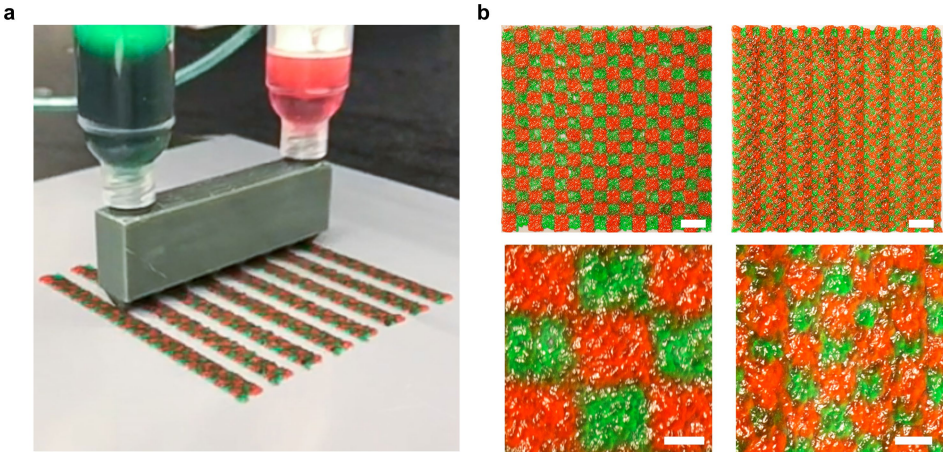

Extended Data Fig. 8 | MM3D printing of gelatin hydrogels. a, Photograph of an MM3D printhead ($N = 8 \times 1$, $S_{ink} = 2$) printing two 7.5% gelatin inks dyed with red and green food colouring. **b**, A parallel-print-path strategy is used to manufacture gelatin chequerboards with square sizes of 4 mm × 4 mm (left) and 2 mm × 2 mm (right). Scale bars: top row, 8 mm; bottom row, 2 mm.

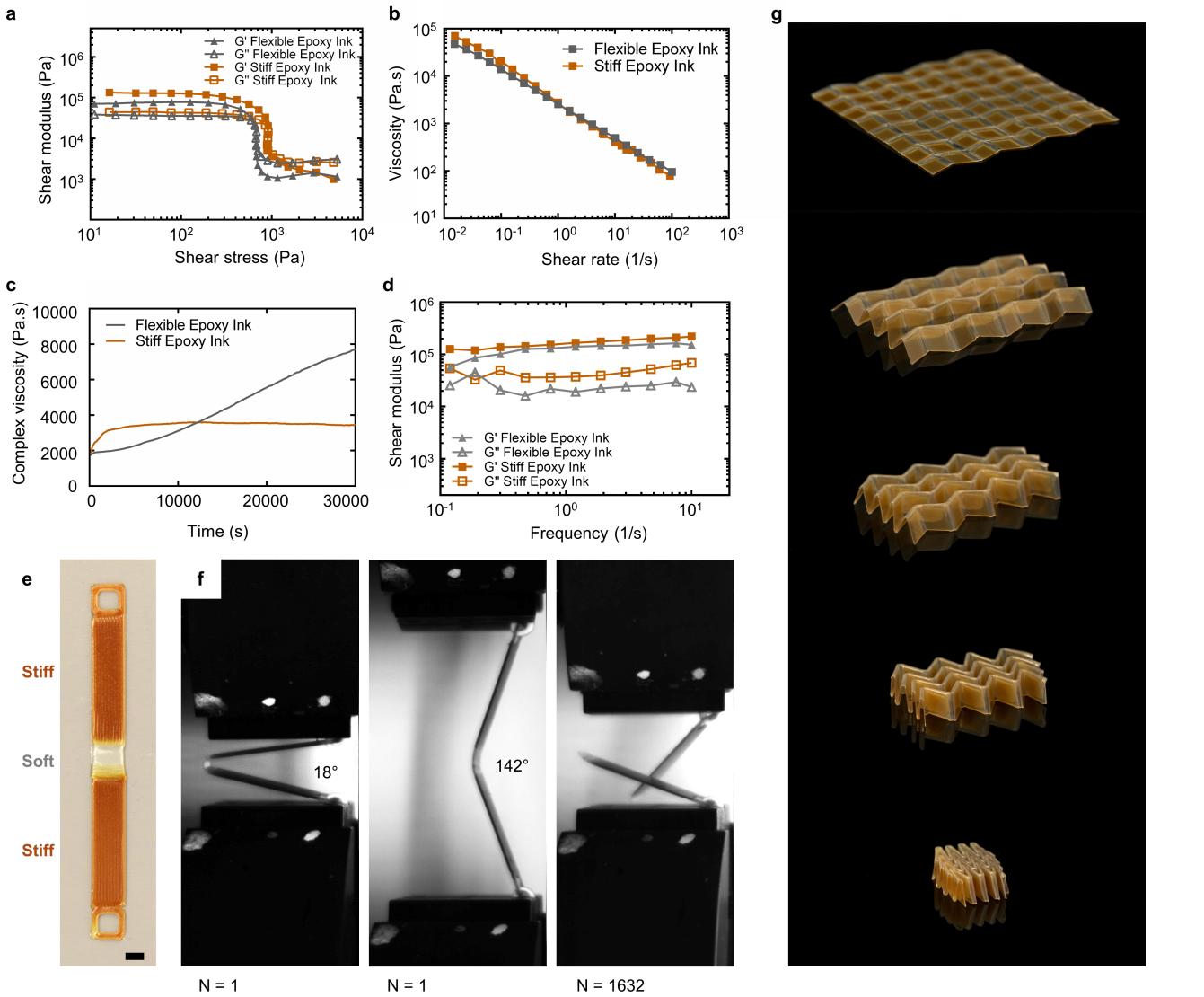

Extended Data Fig. 9 | Rheology, mechanical testing and MM3D printing of flexible and stiff epoxy inks. a, Storage (G') and loss (G'') moduli versus shear stress for flexible (grey) and stiff (orange) epoxy inks. **b**, Apparent viscosity of flexible (grey) and stiff (orange) epoxy inks as a function of shear rate. **c**, Complex viscosity of flexible (grey) and stiff (orange) epoxy inks measured over time using a rheometer at room temperature. **d**, Storage and loss moduli of flexible (grey) and stiff (orange) epoxy inks as a function of frequency. **e**, Photograph of a printed epoxy (flexible) hinge that connects two printed epoxy (stiff) regions. Scale bar, 2 mm. **f**, Cyclic tests carried out at a frequency of 0.5 Hz with bending angles ranging from 18° to 142°. The results reveal that the material can sustain 1,632 ± 217 (mean ± s.d., $n = 6$) cycles before failing. (We note that failure is observed to occur within the flexible epoxy hinge, not at the stiff–soft interfaces.) **g**, Image sequence generated from multiple photographs of a Miura fold at various steps of folding (expanded side length, 64 mm).

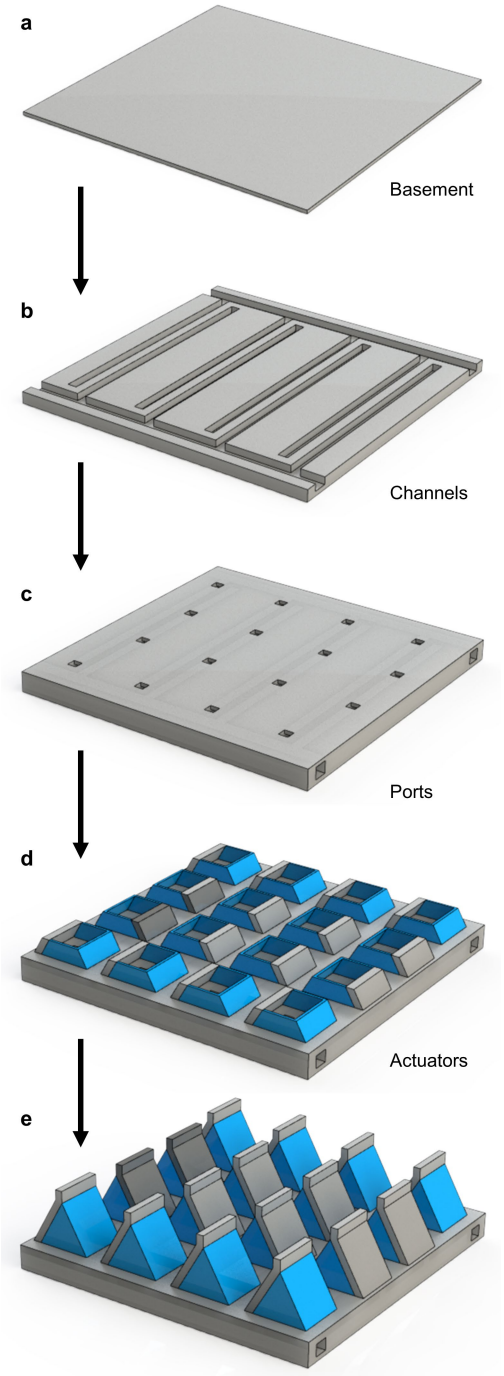

Extended Data Fig. 10 | Printing steps used to create a soft-robotic millipede walker module. a, An air-tight solid basement (two layers) is printed using stiff (grey) elastomeric ink. **b**, A pneumatic channel network is created that connects the vacuum inlets to the actuators (five layers). **c**, The pneumatic channels are embedded and ports are printed that connect the channels to the actuators (three layers). **d**, Actuators are printed on top of the ports using stiff (grey) and flexible (blue) silicone inks. **e**, View of the completed millipede walker module. Each printed layer is 0.5 mm in height and the overall dimensions of each actuator unit are 12 mm × 12 mm × 17 mm.